

Generalised diagnostic framework for rapid battery degradation quantification with deep learning

Ruan, H., Chen, J., Ai, W. & Wu, B

Published PDF deposited in Coventry University's Repository

Original citation:

Ruan, H, Chen, J, Ai, W & Wu, B 2022, 'Generalised diagnostic framework for rapid battery degradation quantification with deep learning', *Energy and AI*, vol. 9, 100158.

<https://doi.org/10.1016/j.egyai.2022.100158>

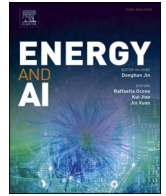
DOI 10.1016/j.egyai.2022.100158

ISSN 2666-5468

Publisher: Elsevier

This is an open access article under the CC BY license

Funding Info - This work was kindly supported by the Faraday Institution's Industrial Fellowship (FIIF-013), Innovate UK Battery Advanced for Future Transport Applications (BAFTA) project (104428), the EPSRC Faraday Institution's Multi-Scale Modelling Project (EP/S003053/1, grant number FIRG003), the EPSRC Joint UK-India Clean Energy centre (JUICE) (EP/P003605/1) and the EPSRC Integrated Development of Low-Carbon Energy Systems (IDLES) project (EP/R045518/1).



Research paper



Generalised diagnostic framework for rapid battery degradation quantification with deep learning

Haijun Ruan^{a,*}, Jingyi Chen^a, Weilong Ai^{a,b}, Billy Wu^{a,b,*}

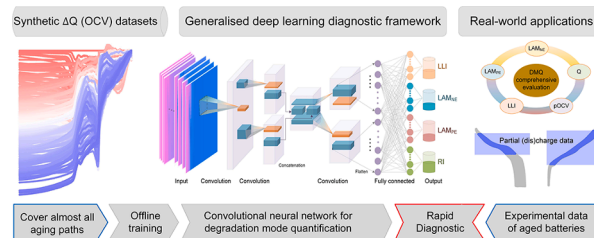
^a Dyson School of Design Engineering, Imperial College London, London, SW7 2AZ, United Kingdom

^b The Faraday Institution, Quad One, Harwell Science and Innovation Campus, Didcot, United Kingdom

HIGHLIGHTS

- A generalised and rapid diagnostic approach with almost all the aging paths presented.
- Lower training cost/time via synthetically generated aging datasets.
- Systematically explored battery degradation theory.
- Validated with three leading battery chemistries aged under different conditions.
- Online real-world application potential highlighted with partial (dis)charge data.

GRAPHICAL ABSTRACT



ARTICLE INFO

Keywords:

Lithium-ion battery
Degradation diagnostics
Deep learning
Battery degradation theory
Synthetic training dataset
Aging paths

ABSTRACT

Diagnosing lithium-ion battery degradation is challenging due to the complex, nonlinear, and path-dependent nature of the problem. Here, we develop a generalised and rapid degradation diagnostic method with a deep learning-convolutional neural network that quantifies degradation modes of batteries aged under various conditions in 0.012 s without feature engineering. Rather than performing extensive aging experiments, synthetic aging datasets for network training are generated. This dramatically lowers training cost/time, with these datasets covering almost all the aging paths, enabling a generalised degradation diagnostic framework. We show that the five thermodynamic degradation modes are correlated, and systematically elucidate their correlations. We thus propose a non-invasive comprehensive evaluation method and find the degradation diagnostic errors to be less than 1.22% for three leading commercial battery chemistries. The comparison with the traditional diagnostic methods confirms the high accuracy and fast nature of the proposed approach. Quantification of degradation modes with the partial discharge/charge data using the proposed diagnostic framework validates the real-world feasibility of this approach. This work, therefore, enables the promise of online identification of battery degradation and efficient analysis of large-data sets, unlocking potential for long lifetime energy storage systems.

1. Introduction

Lithium-ion batteries are currently used in a wide range of

applications including portable electronics, electric vehicles and grid-scale electrical storage due to their ideal energy/power density, decreasing cost and acceptable lifetime [1,2]. However, whilst advances in extending battery lifetime have been made, improvements are still

* Corresponding authors.

E-mail addresses: hruan@imperial.ac.uk (H. Ruan), billy.wu@imperial.ac.uk (B. Wu).

<https://doi.org/10.1016/j.egyai.2022.100158>

Nomenclature	
BMS	Battery management system
CNN	Convolutional neural network
CC	Constant current
DM	Degradation mode
DMQ	Degradation mode quantification
DTV	Differential thermal voltammetry
DV	Differential voltage
EIS	Electrochemical impedance spectroscopy
FC	Full cell
GPR	Gaussian process regression
IC	Incremental capacity
LAM	Loss of active material
LAM _{deNE}	LAM of the delithiated NE
LAM _{dePE}	LAM of the delithiated PE
LAM _{liNE}	LAM of the lithiated NE
LAM _{liPE}	LAM of the lithiated PE
LLI	Loss of lithium inventory
LSTM	Long short-term memory network
MAD	Maximum absolute deviation
MAE	Maximum absolute error
ML	Machine learning
NE	Negative electrode
NMC	LiNi _x Mn _y Co _{1-x-y} O ₂
NN	Neural network
OCV	Open circuit voltage
PE	Positive electrode
pOCV	pseudo-OCV
pR	pseudo reference
ΔQ	Capacity difference
RI	Resistance increase
RMSD	Root mean square deviation
RMSE	Root mean square error
SEI	Solid electrolyte interphase
SEM	Scanning electron microscopy
SOC	State of charge

needed especially under high current and temperature operating conditions [3,4]. Understanding battery degradation is thus of great importance yet challenged by the fact that the underpinning processes are generally complex, non-linear and path-dependent, with different potential causes including lithium plating, particle cracking and growth of the solid electrolyte interphase (SEI) just being a few potential causes [2-3,5-7]. Therefore, decoupling the degradation mechanism and diagnosing battery health is critical for intelligent control to achieve a long lifetime battery system.

In order to investigate battery degradation, many studies have conducted postmortem characterization, which uses spectroscopic techniques such as X-ray diffraction [8,9], and imaging techniques such as scanning electron microscopy (SEM) [10,11]. These tools are extremely useful, however they generally involve the disassembly of the batteries and rely on expensive equipment. Non-invasive diagnostic methods use easy to measure variables, such as voltage/current, and thus are attractive for deployment on real-world battery management systems (BMS) [12]. Various metrics can be inferred from the voltage-current data with the simplest description of battery degradation being capacity fade, which is the ratio of the accessible capacity to the original capacity [5,7,12]. However, whilst this metric is easy to calculate, it overly simplifies the coupled contributions of the negative electrode (NE) and the positive electrode (PE). A more accurate description of these degradation modes (DM) is thus: the loss of lithium inventory (LLI), loss of active material (LAM) of the (de)lithiated NE (LAM_{deNE}, LAM_{liNE}), LAM of the (de)lithiated PE (LAM_{dePE}, LAM_{liPE}), and resistance increase (RI) [13-15].

These states can be inferred from the measurement of the full cell (FC) open circuit voltage (OCV) and with knowledge of the half-cell OCVs [13-16]. However, parameterization of the FC OCV can involve expensive computation due to the non-convex optimization problem and need to iterate calculations when fitting models, which limits its potential deployment on embedded systems and for the analysis of large datasets. In lab-based environments, transformations of the OCV and temperature data, have been proven to be a useful diagnostic tool. This includes incremental capacity (IC) [7,14,17,18], differential voltage (DV) [19,20], and differential thermal voltammetry (DTV) [21, 22] analysis, which can decouple DMs. However, numerical differentiation can decrease the signal-to-noise ratio, and subsequently, a high level of filtering is usually required, highlighting the challenge with the use of these tools in real-world applications. On the other hand, previous studies [15,23] highlighted that some combinations of DMs could lead to the same OCV signals, but did not explore the underlying aspects of

this in detail.

Recently, machine learning (ML) has attracted significant attention for battery applications [24,25]. Gaussian process regression (GPR) [26], neural networks (NN) [27], convolutional NNs (CNN) [28], and long short-term memory network (LSTM) [29] are just a few examples of techniques employed for battery state-estimation and forecasting. In many of the previous works, capacity measurements have been used to train various approaches with reasonable accuracy, however, deeper mechanistic understanding is lacking. Previous work has shown that synthetic DMs can be identified through the use of the ML techniques such as NNs [30], and random forest [31], however, these approaches often require manual feature selection and accurate quantification of the DMs over the lifetime of the cells remains challenging. Tian et al. [32] demonstrated this approach by estimating LAM using a CNN approach, however this method was developed with batteries degraded under the same cycling conditions and thus it is uncertain whether the technique is equally applicable over a range of different conditions. Given the diverse degradation paths, a major challenge in ML-based diagnostics is the large number of aging experiments required for training, resulting in significant time/experiment needs. Synthetic data generation has therefore been proposed as a means of addressing this issue [33,34], however only a limited number of involved aging paths have so far been investigated.

In this work, we propose a rapid and generalised ML-based degradation diagnostic method that can quantify DMs of leading commercial battery chemistries cycled under different conditions in 0.012 s without feature engineering. The capacity difference (ΔQ) of OCVs is used to decouple degradation modes because it does not require numerical differentiation and relevant filtering. Training data is generated synthetically from an OCV model which covers billions of possible DM combinations, thus addressing the time-consuming and experiment-intensive issues for training dataset generation. Furthermore, we prove that any four thermodynamic DMs are not independent, and systematically explore their interdependencies; extending battery degradation theory. To the best of the authors' knowledge, this is the first time these interdependencies have been comprehensively elucidated. We have thus formulated a non-invasive comprehensive evaluation method capable of assessing the diagnostic accuracy of individual DMs, and find the quantification errors of all the thermodynamic DMs for the three main battery chemistries are less than 1.22%. The proposed method exhibits a promising potential of real-world applications as it quantifies the DMs accurately with partial discharge/charge data, with the computational efficiency needed to analyze large datasets.

The remaining part of this paper is organized as follows. Battery degradation theory is explored in Section 2 and the generalised degradation diagnostic framework for rapid battery degradation quantification is developed in Section 3. Section 4 gives the quantification results of battery degradation modes and Section 5 discusses the comparison and real-world application potential of the proposed method, followed by conclusions summarized in Section 6. All the details about the proposed approach are elaborated in Methods Section 7.

2. Battery degradation theory

2.1. Independence and correlation of degradation modes

$$\text{OCV}_{\xi_{\text{LAM}_{\text{deNE}}} + \xi_{\text{LAM}_{\text{LiPE}}}} = \text{OCV}_{\xi_{\text{LAM}_{\text{LiNE}}} + \xi_{\text{LAM}_{\text{dePE}}}}; \text{s.t. } \xi_{\text{LAM}_{\text{deNE}}} = \xi_{\text{LAM}_{\text{LiNE}}} = \xi_{\text{LAM}_{\text{dePE}}} = \xi_{\text{LAM}_{\text{LiPE}}} \quad (3)$$

The six common DMs can generally be categorized as either thermodynamic metrics: LLI, LAM_{LiNE} , LAM_{deNE} , LAM_{LiPE} , LAM_{dePE} , or a

kinetic metric: RI [13-14,16], with all these having a measurable effect on the FC pseudo-OCV (pOCV, Supplementary Fig. 1). However, these are not independent, particularly for the five thermodynamic DMs; with certain combinations creating the same pOCVs. This indicates that the five thermodynamic DMs are correlated and some of them can be identical to others, from the perspective of their pOCVs. The identical pOCVs can thus be expressed as:

$$\text{OCV}_{\xi_{\text{LLI}} + \xi_{\text{LAM}_{\text{deNE}}}} = \text{OCV}_{\xi_{\text{LAM}_{\text{LiNE}}}}, \text{s.t. } \xi_{\text{LAM}_{\text{deNE}}} = \xi_{\text{LAM}_{\text{LiNE}}} = \xi_{\text{LLI}} \quad (1)$$

$$\text{OCV}_{\xi_{\text{LLI}} + \xi_{\text{LAM}_{\text{dePE}}}} = \text{OCV}_{\xi_{\text{LAM}_{\text{LiPE}}}}, \text{s.t. } \xi_{\text{LAM}_{\text{dePE}}} = \xi_{\text{LAM}_{\text{LiPE}}} = \xi_{\text{LLI}} \quad (2)$$

Here ξ represents the amount of each DM. When the amounts of LAM_{deNE} , LLI, and LAM_{LiNE} are identical, any combination of LLI and

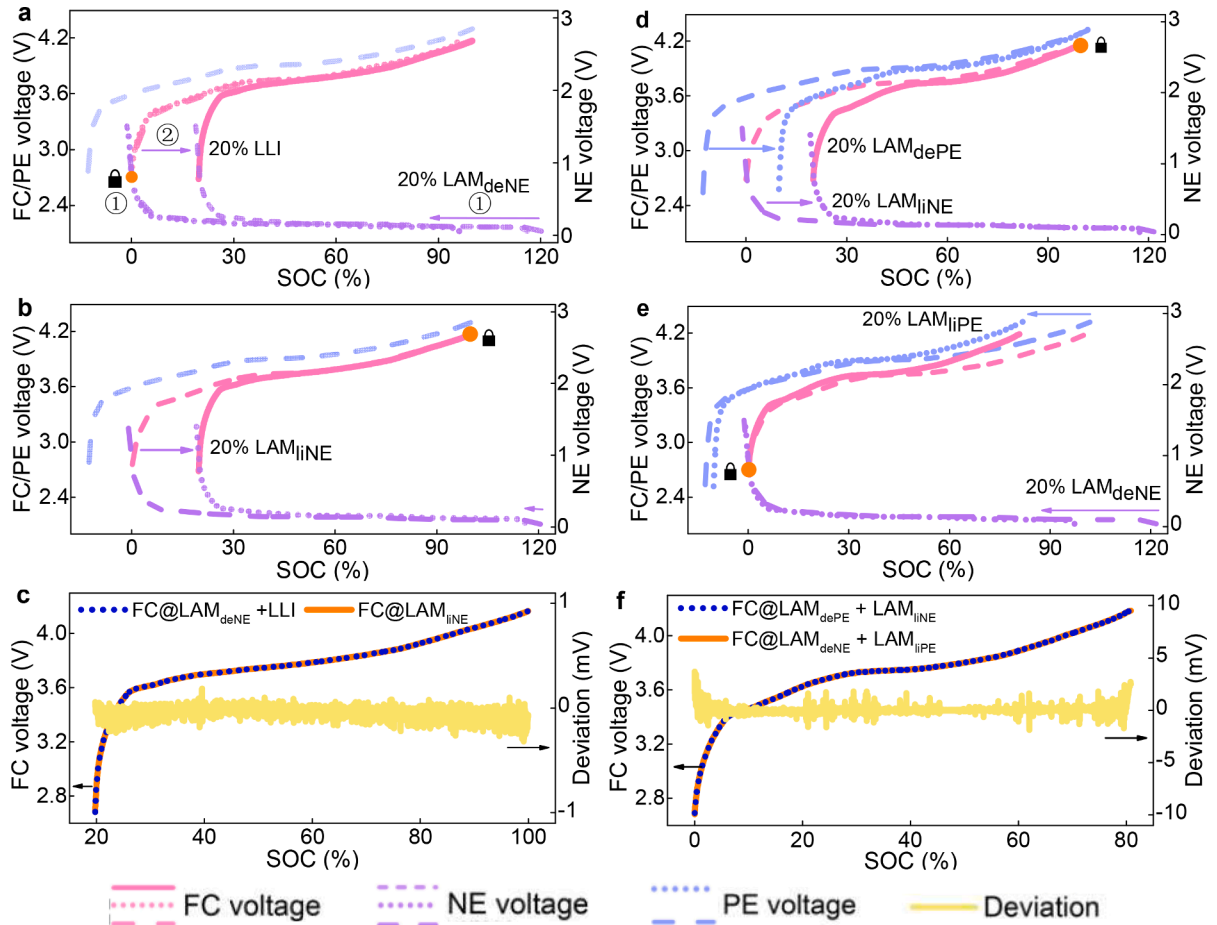


Fig. 1. Correlation of basic DMs**. A typical illustration of FC pOCVs created by a combination of LLI and LAM_{deNE} , and LAM_{LiNE} for a representative $\text{LiNi}_x\text{Mn}_y\text{Co}_{1-x-y}\text{O}_2/\text{Graphite}$ battery (termed as NMC). **a**, FC pOCV caused by 20.0% LAM_{deNE} and 20.0% LLI. **b**, FC pOCV caused by 20.0% LAM_{LiNE} . **c**, The comparison of these two FC pOCVs under different states of charge (SOCs). The root mean square deviation (RMSD) and maximum absolute deviation (MAD) between them are 0.08 mV and 0.32 mV, respectively. A typical illustration of FC pOCVs created by a combination of LAM_{LiNE} and LAM_{dePE} , and a combination of LAM_{deNE} , and LAM_{LiPE} for a representative NMC battery. **d**, FC pOCV caused by 20.0% LAM_{LiNE} and 20.0% LAM_{dePE} . **e**, FC pOCV caused by 20.0% LAM_{deNE} and 20.0% LAM_{LiPE} . **f**, The comparison of these two FC pOCVs, where the FC pOCV in Fig. 1d is shifted to the same start SOC point as that in Fig. 1e. The RMSD and MAD between the two pOCVs are 0.31 mV and 3.71 mV, respectively. In Fig. 1a, ① represents the first step that there is 20.0% LAM_{deNE} , and the FC pOCV caused by 20.0% LAM_{deNE} is created. ② represents the second step that there is 20.0% LLI after 20.0% LAM_{deNE} , and the FC pOCV caused by 20.0% LAM_{deNE} and 20.0% LLI is created. The half-cell pOCVs of PE and NE are displayed to understand the creation of FC pOCVs through their scaling and/or shifting.

LAM_{deNE} creates the same pOCV as LAM_{liNE} (Eq. (1), Fig 1a-c, and Supplementary Fig. 3). The same holds true for any combination of LLI and LAM_{dePE}, and LAM_{liPE} (Eq. (2), and Supplementary Figs. 2–3). This is fundamentally because the aged FC pOCV, caused by lithiated LAM, can also be obtained by superposing the same LLI and delithiated LAM (Supplementary Note 1). Furthermore, any combination of LAM_{deNE}, and LAM_{liPE} can create the same pOCV as that of LAM_{liNE}, and LAM_{dePE} (Eq. (3), Fig. 1d-f), when the loss of these four DMs are identical, which can be deduced by combining Eq. (1) and Eq. (2). Ultimately, there are many other combinations of thermodynamic DMs that can create the same pOCVs by transforming Eq. (1), Eq. (2) and Eq. (3) (Supplementary Note 2). Therefore, we can conclude that any four thermodynamic DMs are not independent.

2.2. Correlation of the combinations of independent degradation modes

The maximum number of thermodynamic DMs to ensure independence is thus three. To investigate this further, combinations of three independent thermodynamic DMs and one kinetic DM are used to create four scenarios (Sc1, Sc2, Sc3 and Sc4, See Fig. 2a), with the four DMs in each scenario creating unique pOCVs. The LLI is considered in each scenario because it often occurs during battery aging [2-3,5,7-17, 20-23]. With this, any battery can be diagnosed with the four independent DMs in each scenario (Fig. 2b). If Sc1 is taken as an example, LLI, LAM_{deNE}, LAM_{dePE}, and RI can be directly identified, and LAM_{liNE} and LAM_{liPE} would be taken as a combination of LLI and LAM_{deNE}, and a combination of LLI and LAM_{dePE}, respectively (Fig. 2b). Thus, the identified LLI does not generally represent pure LLI. The amounts of

quantified LAM_{deNE} and LAM_{dePE} could be identical as the sum of LAM_{deNE} and LAM_{liNE}, and the sum of LAM_{dePE} and LAM_{liPE}, respectively. This illustrates that the identification of LLI, LAM_{deNE}, and LAM_{dePE} is generally a pseudo quantification. The same holds true for the DM quantification (DMQ) in Sc2, Sc3, and Sc4 (Fig. 2). Consequently, a corollary can be obtained as:

$$\begin{cases} \xi_{LAME} = \xi_{LAMNE_1} = \xi_{LAMNE_2} = \xi_{LAMNE_3} = \xi_{LAMNE_4} \\ \xi_{LAME} = \xi_{LAMPE_1} = \xi_{LAMPE_2} = \xi_{LAMPE_3} = \xi_{LAMPE_4} \\ \xi_{RI} = \xi_{RI_1} = \xi_{RI_2} = \xi_{RI_3} = \xi_{RI_4} \end{cases} \quad (4)$$

where subscript 1, 2, 3, and 4 represent Sc1, Sc2, Sc3, and Sc4, respectively. This suggests that the amounts of quantified LAM_{NE}, LAM_{PE} and RI in the four scenarios would be the same (Fig. 2a), respectively. The identified LLI in the four scenarios would generally be different and a corollary for the quantified LLI can be deduced as:

$$\begin{cases} \xi_{LLI_1} - \xi_{LLI_3} = \xi_{LLI_4} - \xi_{LLI_2} = \xi_{LAMNE} \\ \xi_{LLI_1} - \xi_{LLI_4} = \xi_{LLI_3} - \xi_{LLI_2} = \xi_{LAMPE} \\ \xi_{LLI_1} - \xi_{LLI_2} = \xi_{LAMNE} + \xi_{LAMPE} \\ \xi_{LLI_1} + \xi_{LLI_2} = \xi_{LLI_3} + \xi_{LLI_4} \\ \xi_{LLI_1} \geq \xi_{LLI_3} \geq \xi_{LLI_2}; \xi_{LLI_1} \geq \xi_{LLI_4} \geq \xi_{LLI_2} \\ \xi_{LLI_1} \geq \xi_{LLI_{pure}} \geq \xi_{LLI_2} \end{cases} \quad (5)$$

This indicates that the identified LLI in the four scenarios are correlated, and they are also related to the identified LAM. These correlations are primarily because the identified LLI in each scenario is generally not pure LLI but usually involves the contribution from the LAM.

The quantified LLI₁ would be the maximum, generally higher than

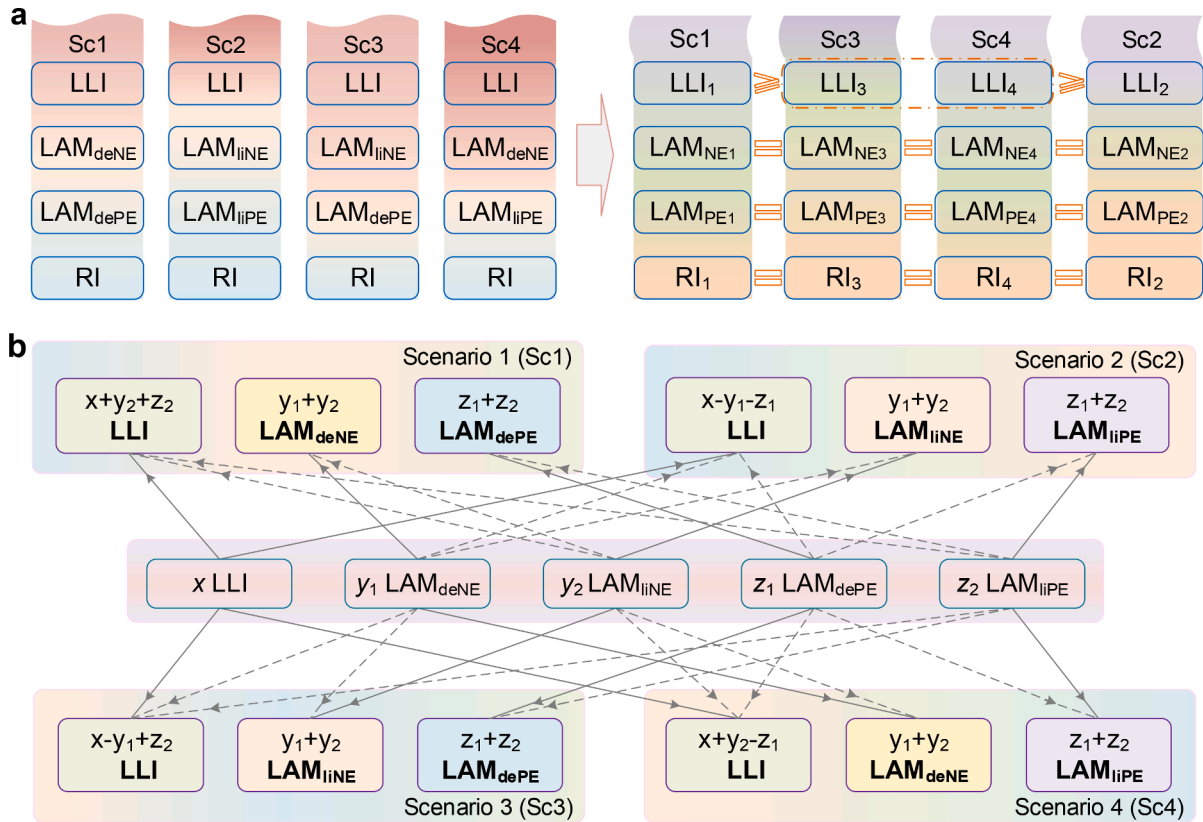


Fig. 2. Combinations of independent DMs and their correlations. **a**, Combinations of independent DMs in four scenarios: Sc1, Sc2, Sc3 and Sc4. In each scenario, to simplify the nomenclature, the DMs are directly written as LLI_i, LAM_{NEi}, LAM_{PEi}, and RI_i, where *i* represents Sc1, Sc2, Sc3, or Sc4. **b**, The illustration of battery degradation diagnostics with four independent DMs in each scenario. The solid lines represent the direct identification, while the dash lines represent the indirect identification with the transformation from lithiated LAM (delithiated LAM) into delithiated LAM and LLI (lithiated LAM and LLI). It is assumed that there are *x* LLI, *y*₁ LAM_{deNE}, *y*₂ LAM_{liNE}, *z*₁ LAM_{dePE}, *z*₂ LAM_{liPE}, and *m* RI in one battery. In the Sc1, as an example, *x* LLI, *y*₁ LAM_{deNE}, *z*₁ LAM_{dePE}, and *m* RI in the battery can be directly quantified (shown with solid lines), while *y*₂ LAM_{liNE} and *z*₂ LAM_{liPE} would be taken as *y*₂ LLI and *y*₂ LAM_{deNE}, and *z*₂ LLI and *z*₂ LAM_{dePE}, respectively (shown with dash lines). There would be *x* + *y*₂ + *z*₂ LLI, *y*₁+*y*₂ LAM_{deNE}, *z*₁ + *z*₂ LAM_{dePE}, and *m* RI in the Sc1.

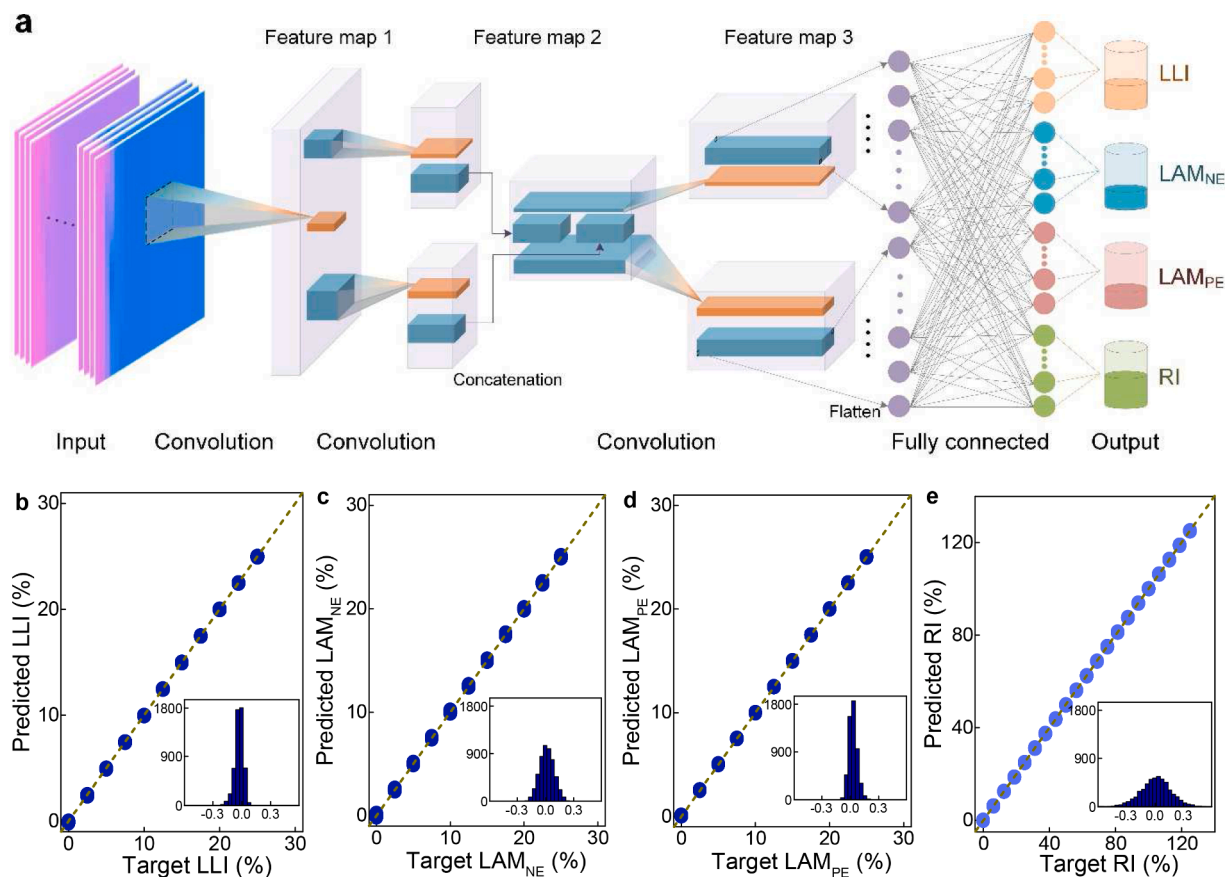


Fig. 3. Convolutional neural network for degradation mode quantification**. a, The network architecture of the CNN for DMQ. Capacity differences of pOCVs as a function of voltage, $\Delta Q(V)$, are transformed to 2D images and used as the CNN input. When drawing input figures, the values of the second and third channels are set as 0.5 and 1, respectively. The four outputs correspond to four independent DMs with different quantified values. More details of the CNN are exhibited in the ‘Methods’ section. The testing results of CNN using randomly 20% of synthetic dataset in the Sc1 for a representative NMC battery, i.e. the predicted and target values of b, LLI c, LAM_{NE} d, LAM_{PE} e, RI. The inset shows the histogram of residuals (predicted - target) for the testing dataset (5304 data points).

the pure LLI, and represents the total LLI within the battery, including both the lithium lost through pure LLI and the lithium lost in lithiated active materials. Therefore, the DMs in Sc1 represent the finalized DMQ result for battery diagnostics, i.e. LLI, LAM_{NE}, LAM_{PE}, and RI.

3. Generalised degradation diagnostic framework

In order to quantify the four independent DMs (LLI, LAM_{NE}, LAM_{PE}, and RI), a deep learning, CNN approach was adopted (Fig. 3a). The CNN can extract features automatically by learning from the raw data, instead of relying on the manual extraction of degradation features. Here, the capacity differences ($\Delta Q(V)$) between the aged pOCVs and the fresh pOCV as a function of voltage were taken as the CNN input, where the $\Delta Q(V)$ data was transformed into a 2D matrix, equivalent to a 2D image (see Methods and Supplementary Fig. 4). $\Delta Q(V)$ is a relatively reliable signal to manifest the evolution of aged pOCVs, because it does not require the numerical differentiation that usually amplifies noise, and which suffers from the need for a high level of filtering, reducing potential information loss due to overfitting/underfitting [24,35]. All the training data for the CNN are synthesized based on an OCV model using the half-cell potential of the NE and PE with different DMs (see Methods and Supplementary Fig. 4). This removes the need to conduct time-consuming degradation experiments (generally taking many months or even several years [4, 24]) for training the CNN. Consequently, the experimental cost and training time is extremely low and the development time of the CNN-based diagnostic method is short (Several hours), when training the CNN with the synthetic data. Here, the key element is the high-fidelity OCV model, which is parameterized

by considering not only the OCV error but also the IC and DV errors (see Methods). This aids accuracy by focusing on spectra that are more sensitive to PE and NE processes, respectively. Furthermore, the synthesized training datasets can include almost all potential aging paths, representing more than 1 billion possibilities (Supplementary Note 3). This enables the formulation of a generic CNN-based diagnostic method that can quantify DMs of batteries aged under various conditions.

4. Results

4.1. Degradation diagnostics and comprehensive evaluation with synthetic aging data

Fig. 3b-e presents the testing results of the trained CNN in Sc1 using a random 20% sample of the synthetic data for a representative NMC battery. The predicted DMs match well with the target DMs, with a root mean square error (RMSE) and maximum absolute error (MAE) of less than 0.16% and 0.61%, respectively (Supplementary Table 1). Further testing results for the trained CNNs in different scenarios for different battery chemistries (LiFePO₄/Graphite, termed as LFP; LiNi_xCo_yAl_{1-x-y}O₂/Graphite, termed as NCA) show that the RMSEs are less than 0.20% for the thermodynamic DMs (Supplementary Table 1, and Supplementary Fig. 5). The excellent testing results demonstrate that the trained CNN can accurately capture target DMs.

To further validate the CNN model, we assumed an NMC battery degrades with aging path I (Supplementary Fig. 6 and Supplementary Note 3), and then generated the corresponding pOCVs (Supplementary Fig. 7). Using the trained CNN, we can quantify the DMs of this battery,

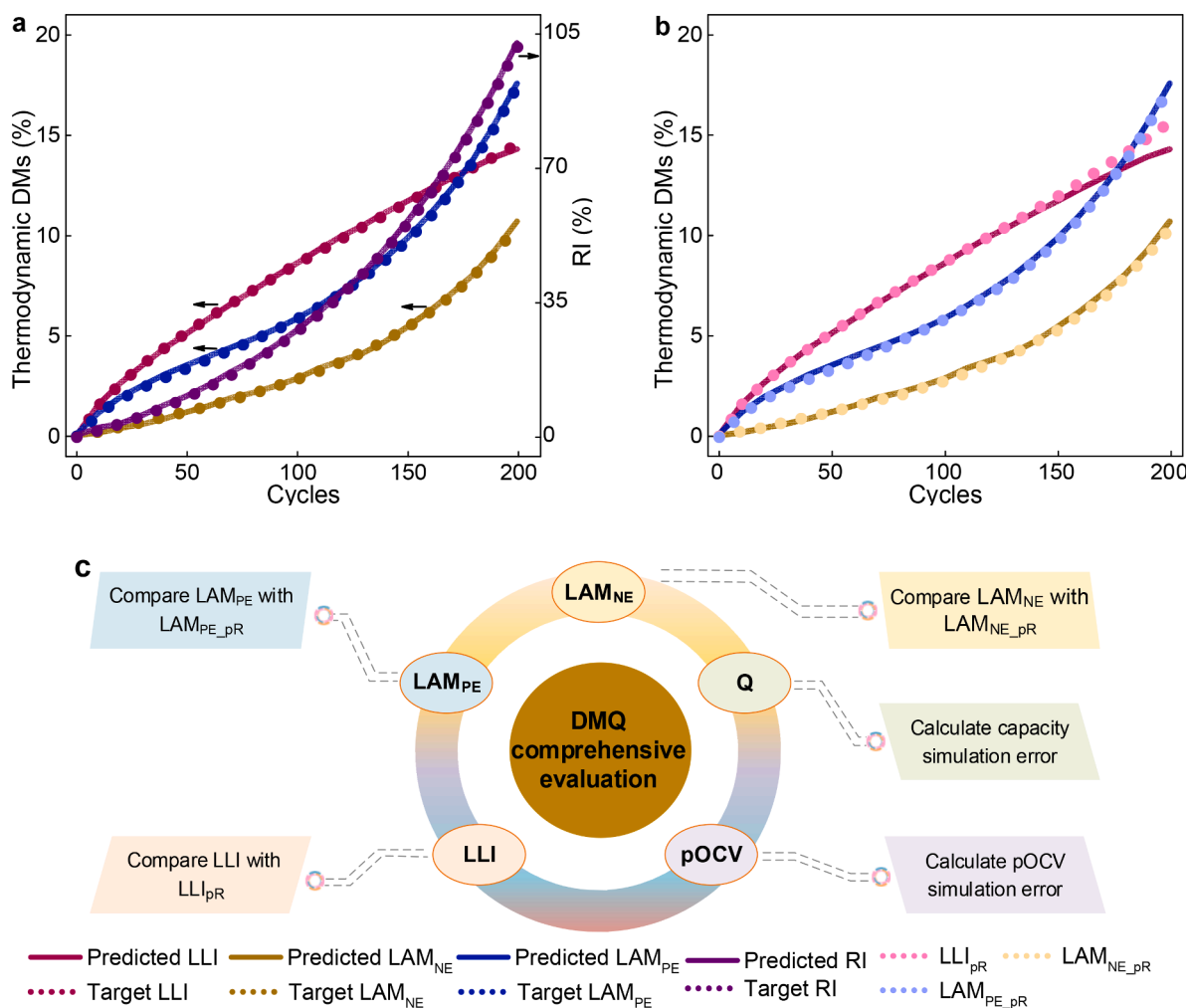


Fig. 4. Degradation diagnostics and comprehensive evaluation with synthetic aging data**. a, The quantified DMs, LLI, LAM_{NE}, LAM_{PE}, and RI, with synthetic NMC battery data using the CNN in Sc1 and target DMs. The solid and dot lines represent the predicted and target DMs, respectively. b, The quantified DMs, LLI, LAM_{NE}, LAM_{PE}, and the pseudo reference (pR) DMs, LLI_{pR}, LAM_{NE,pR}, LAM_{PE,pR}. The dot lines represent the pR DMs. c, Illustration of the DMQ comprehensive evaluation method with five metrics, i.e. LLI, LAM_{NE}, and LAM_{PE}, pOCV, and capacity (Q). The pOCV and Q metrics are represented by the pOCV and Q simulation errors, while the quantified LLI, LAM_{NE}, and LAM_{PE} would be compared with the corresponding pR ones which are calculated from the identified DMs in Sc2, Sc3 and Sc4. More details of the comprehensive evaluation method are exhibited in the ‘Methods’ section.

Table 1
The DMQ errors for the three batteries compared with the target ones and from the comprehensive evaluation.

		Compared with the target ones				From the comprehensive evaluation				
		LLI	LAM _{NE}	LAM _{PE}	RI	pOCV	Q	LLI	LAM _{NE}	LAM _{PE}
RMSE (%)	NMC	0.09	0.09	0.04	0.22	0.07	0.06	0.45	0.11	0.08
	LFP	0.56	0.05	0.07	0.31	0.27	0.25	0.99	0.07	0.06
	NCA	0.21	0.07	0.06	0.23	0.21	0.61	0.79	0.04	0.07

as presented in Fig. 4a, with inferred DMs matching well and having a RMSE of less than 0.22%. Further quantification for LFP and NCA batteries under the aging path II and III (Supplementary Fig. 6, and Supplementary Note 3) are presented in Supplementary Fig. 8. Again, the excellent quantification results (RMSE<0.56%, Table 1) illustrate that the trained CNN can accurately and robustly quantify DMs of batteries degraded under different aging paths, due to the richness of the synthetic training data.

For batteries cycled in real-world conditions, it is challenging to know what the actual contributions from the DMs are. Only using the OCV simulation error is not sufficient to evaluate the accuracy of quantified DMs in some cases (Supplementary Note 4). We thus propose a non-invasive comprehensive evaluation method that can

systematically assess the DMQ results (Fig. 4b-c, Methods), based on the developed DM corollary (proved in Supplementary Note 5). This not only adopts the measurement pOCV and capacity but also the pseudo reference (pR) DMs, which are calculated from the identified DMs in the other three scenarios (see Methods, e.g. LAM_{PE,pR} is the mean of LAM_{PE2}, LAM_{PE3}, and LAM_{PE4}). First, the pOCV and capacity simulation accuracy of the NMC battery is checked, and we find that their RMSEs are less than 0.07% (Table 1, and Supplementary Fig. 12). The quantified LLI, LAM_{NE}, and LAM_{PE} of the NMC battery show good consistency with those corresponding pR DMs (Fig. 4b, Table 1, RMSE<0.45%). Further comprehensive evaluation of the DMQ results for the LFP and NCA batteries was performed, with all the RMSEs less than 0.99% (Table 1, and Supplementary Fig. 12). The comprehensive evaluation results (LLI:

RMSE<0.99%; LAMs: RMSE<0.11%) are comparable with the quantification errors (LLI: RMSE<0.56%; LAMs: RMSE<0.09%) for these three batteries, indicating effective evaluation. This suggests that the comprehensive evaluation method, which leverages the interdependencies of DMs, can indicate the accuracy of the individual DMs to some extent.

4.2. Rapid degradation diagnostics for experimentally aged batteries

The trained CNN can directly quantify the DMs of different battery chemistries aged under various cycling conditions within a short time. The DMQ time for each pOCV measurement is extremely short and less than 0.012 s (Table 2, tested on a single general laptop computer with an Intel(R) Core(TM) i5-4300 U CPU). This enables the potential of online battery degradation diagnostics to guide battery charging and intelligent control for battery lifetime extension.

Fig. 5 presents the DMQ results for three types of leading commercial batteries with different aging paths. Here, there is limited degradation in the NE material of the NMC battery relative to the large amount of PE degradation. This is primarily attributed to the cycling conditions which involved a low charge current (0.3C) and a high discharge current (5C) which was done at a high temperature of 45 °C. The aggressive and repeated intercalation of lithium ions at 5C is likely to cause significant mechanical stress in the PE, leading to particle fracture and also structural decay [36–38]. This is evidenced by the SEM micrographs in Supplementary Fig. 13. A high LLI does occur, mainly due to the SEI growth resulting from the high rate of side reactions associated with the high temperature testing (45 °C) [13-17, 37-38], and from the formation of fresh cathode electrolyte interphase (cathode SEI) as mechanical fracture of PE exposes new particle surfaces to the electrolyte [38]. The SEI growth on the NE and PE is demonstrated by the significant increase of the SEI resistance of the NMC battery [39] (EIS results in Supplementary Fig. 14). These three batteries exhibit resistance increase, highlighting the kinetic degradation with battery aging (Supplementary Figs. 14–16).

The degradation of the retired LFP battery is related to, not only operational conditions during 2nd use, but also the previous aging path, and its degradation mechanisms would thus be more complex. The LAM in both electrodes and LLI increase linearly with cycling, with LAM_{PE} and LLI almost the same. LAM_{PE} of approximately 17% (Supplementary Figs. 3 and 23) is observed in the LFP battery during 1st use, possibly caused by the isolation of, and cracks in, active material particles due to the harsh operation conditions [37-38,40]. The possible mechanical degradation would induce increased aging stress during 2nd use [38,41] and thus leads to the further degradation of the LFP cathode. The large amount of degradation in the graphite electrode happens when cycled at a high charge current (0.5C), which is the maximum permissible charge current for this cell. Rapid intercalation into the graphite particles likely causes crack formation and delamination from the current collector [42, 43]. Particle cracking on the NE and PE electrodes would lead to the new formation of SEI [17, 37,40-43], thus resulting in the LLI.

Despite the similar decreasing capacity trend (Supplementary Fig. 20), the degradation path of the NCA battery is different, where the NE/PE and battery resistance exhibit rapid initial degradation, with this slowing down in subsequent cycles. The long calendar aging time and short cycling time (10 day calendar aging-2 days cycling) is responsible for this phenomenon, with the calendar aging at 90% SOC, which follows square root time relationship [44–46]. The rest periods at high SOC (high voltage) likely cause increased cathodic and anodic side reactions

Table 2

The average computational time of the trained CNN to quantify DMs as per each input for three batteries.

	NMC	LFP	NCA
Time (s)	0.0119	0.0118	0.0088

[38,46,47], and this can happen mostly in the initial period. Before 264 cycles (336 days, Supplementary Fig. 21), the LLI also exhibits a similar increasing trend due to the SEI growth [46,47], however, it then increases rapidly. The principal reason is that the NE does not have enough sites to accommodate lithium ions during charging, and thus lithium plating occurs after the severe fade of the NE [32,48]. This diagnostic suggests that the charging current and/or the upper cut-off voltage must be decreased to prevent lithium deposition, implying the utmost importance of battery and electrode health diagnostics to ensure battery lifetime and safety.

Through comprehensive evaluation of the DMQ results for three battery chemistries, the estimated pOCVs and capacities agree well with the experimental data, with their RMSEs less than 0.63% (Table 3, Supplementary Figs. 17–19). The quantified LLI, LAM_{NE} and LAM_{PE} match well with those corresponding pR ones (calculated with Eqs. (13)–14, see Methods), respectively, and their RMSEs are less than 1.22% (Table 3, Supplementary Figs. 17–19). The quantification errors of the LAM_{PE} for three batteries are relatively low (less than 0.39%), while those of the LAM_{NE} increase a little (less than 0.97%), mainly attributed to the relatively low changes of FC pOCVs under the low LAM_{deNE} (Supplementary Fig. 1). The relatively high evaluation error of the quantified LLI is likely because the pR LLI involves all the identification DM errors in the other three scenarios. The real errors in the quantified LLI for the three batteries are thus generally lower than 1.22%, or even lower than 1%. The low DMQ errors (generally less than 1%) from the non-invasive comprehensive evaluation confirms the high accuracy of the proposed deep learning-based method in quantifying DMs of different batteries aged with different paths.

5. Discussion

5.1. Comparison with OCV model parameterization-based diagnostic method

We highlight the advantages of the proposed method by comparing the CNN approach with an OCV model parameterization-based diagnostic method. The OCV model parameterization approach is commonly carried out with the use of an optimization routine, with methods such as: genetic algorithms [14, 16], gradient based methods such as *fmincon* [15] and particle swarm optimization [49]. Whilst searching through the various potential solutions space (Fig. 6a), many iterations are needed to minimize the objective function, with this process taking many minutes (Table 4). Conversely, only one ‘forward mode’ calculation is needed for the proposed CNN method and thus a short diagnostic time of <0.012 s (Tables 2 and 4) is achieved. As the optimization results may be different with various initial values [15], five optimization processes for the OCV model parameterization are tested, with the RMSEs of all simulation pOCVs less than 9.45 mV (Supplementary Table 4). The diagnostic results under different aging conditions are illustrated in Fig. 6b, and their average values match well with those from the proposed method, having a RMSD less than 0.72%. The comparison indicates that the proposed method achieves high accuracy in an extremely short time.

We also recognize the fact that this approach does require training of the CNN from synthetic data which can take on the order of minutes to hours, however once trained the main benefit of this approach is the aforementioned computational efficiency with a single ‘forward mode’ calculation, which allows for the efficient analysis of large datasets. Furthermore, there is a scope of transfer learning techniques [28,50] to lower this training time, by building on already trained CNNs.

5.2. Real-world application potential

Full discharge/charge cycling is rare in real-world operations and the applicability of techniques with partial discharge/charge data thus necessitates verification. Fig. 7 illustrates the quantified DMs of the NMC

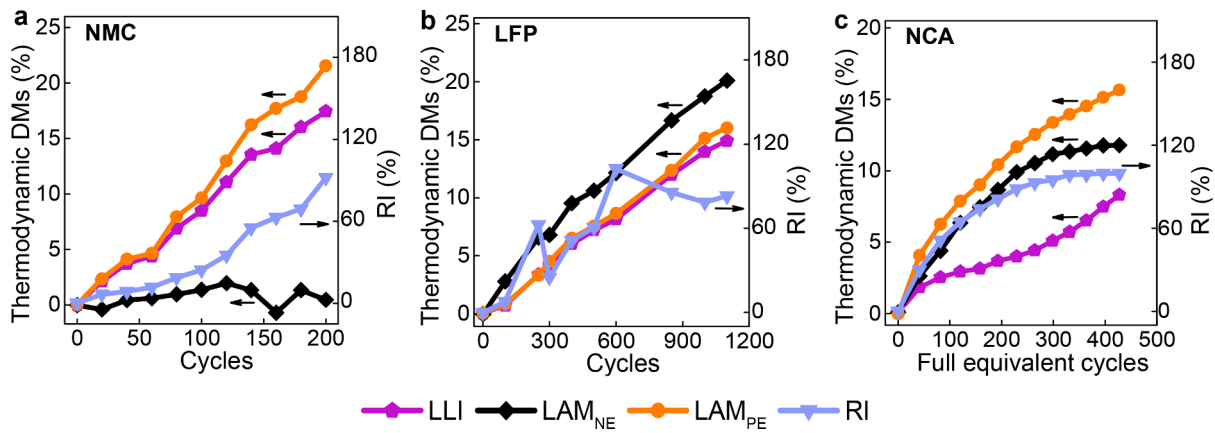


Fig. 5. Degradation modes quantification for three experimentally aged batteries using CNN. The prediction results of DMs using the proposed CNN-based degradation diagnostic method for three types of leading commercial batteries, a, NMC battery cycled with 5C discharge and 0.3C charge at 45 °C; b, the retired LFP battery cycled with 1C discharge and 0.5C charge representing the second use; c, NCA battery with cycling aging (0.5C charge/discharge) and calendar aging (rest at 90% SOC), mimicking the practical applications with periodically calendar aging and charge/discharge aging.

Table 3

The results of the comprehensive evaluation for three types of commercial batteries with five metrics.

RMSE	pOCV (mV)	Q (%)	LLI (%)	LAM _{NE} (%)	LAM _{PE} (%)
NMC	11.48 (<0.42%)	0.38	0.96	0.65	0.32
LFP	11.66 (<0.47%)	0.42	1.22	0.97	0.39
NCA	14.39 (<0.50%)	0.63	1.21	0.64	0.25

and NCA batteries using the CNN, whose training is the same as that described in Section 3 and Methods, with the only difference in the ΔQ (V) of the partial voltage range as input. With the discharge data from 3.55 V to 4.05 V at 0.3C, we find the quantification results match well with those in Fig. 4a, having a RMSD of less than 1.54% (Table 5). For the NCA battery with the charge data from 3.40 V to 4.18 V, the identification results are consistent with those in Fig. 4c, where the RMSD is below 1.75% (Table 5). With the identified DMs, the FC pOCV can be reconstructed with half-cell OCVs, and the RMSEs of calculated pOCVs and capacities of two batteries are less than 1.16% (Table 5, Supplementary Fig. 25). This demonstrates that the proposed method

effectively quantifies the DMs of different aged batteries with partial (dis)charge data, yielding a promising candidate for online diagnostics. Compared with the existing diagnostic methods, such as Lee et al. [30], Mayilvahanan et al. [31], Tian et al. [32], our proposed framework adopts synthetic data for the CNN training, dramatically reducing training cost/time, with the trained CNN featuring the identification of DMs for batteries in different aged conditions.

Table 4

The comparison of diagnostic results for the NMC battery obtained from the OCV model parameterization-based diagnostic method and the proposed CNN method. The computation time is the average value of five calculations for one diagnostic on the same computer (a single general laptop computer with an Intel (R) Core(TM) i5-4300 U CPU).

Computation time (s)		RMSD of quantification results (%)		
OCV model-based method	Proposed method	LLI	LAM _{NE}	LAM _{PE}
1163.0790	0.0119	0.24	0.72	0.53

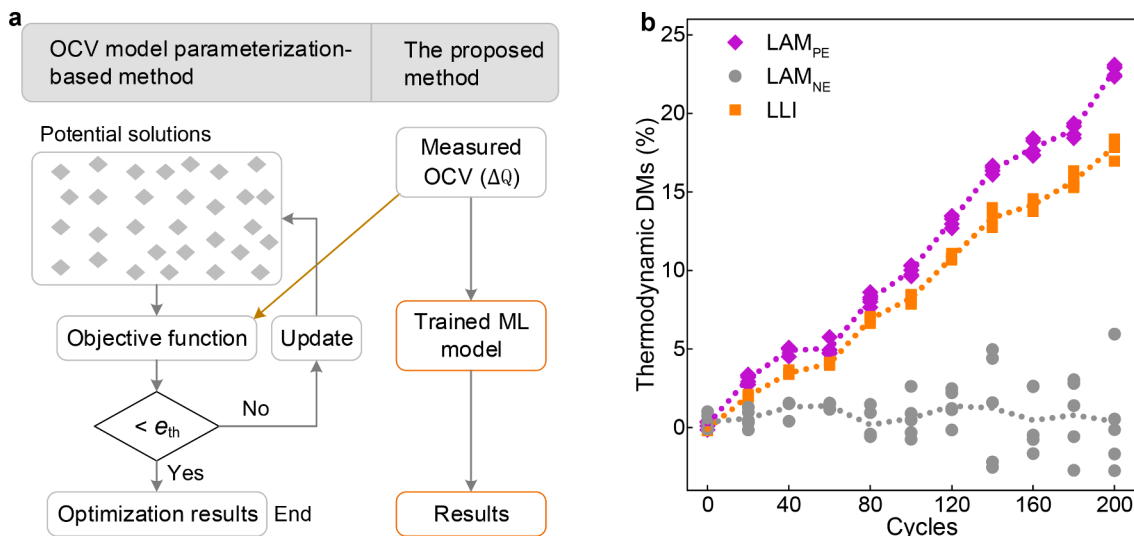


Fig. 6. Comparison between the OCV model parameterization-based diagnostic method and the proposed CNN method**. a, Illustration of the computation process of two diagnostic methods. e_{th} represents the pre-set error threshold for optimization. b, The identification results of the OCV model parameterization-based diagnostic method for the five optimization processes. The diagnostic method refers to [14, 15], and the dotted line represents the average value of each thermodynamic DMs.

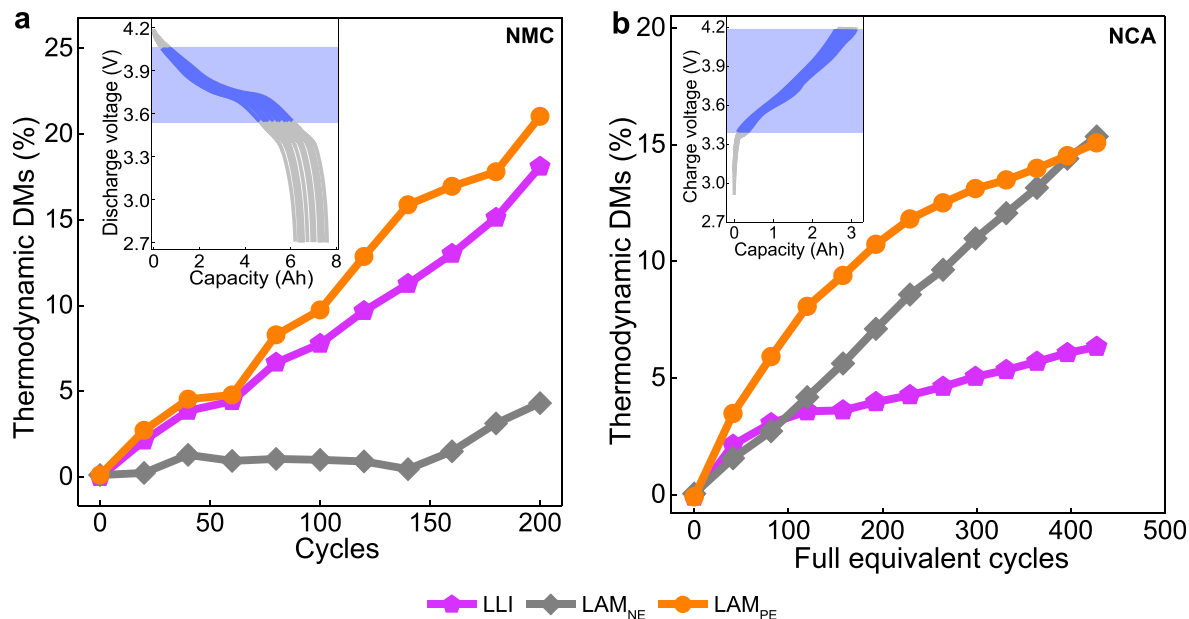


Fig. 7. Degradation mode quantification with partial discharge/charge data using the trained CNN. The diagnostic results of DMs using the proposed CNN-based framework for two batteries a, NMC battery with the partial discharge data between 3.55 V and 4.05 V; b, NCA battery with the partial charge data between 3.40 V and 4.18 V. During training and validation, the partial discharge/charge data with the same voltage range are used for each battery. The inset (blue area) shows the used voltage range.

Table 5

The comparison of diagnostic results (RMSD) between the full and partial discharge/charge data using the CNN. The RMSE shows the comparison of the simulation and experimental pOCVs and capacities.

	RMSD LLI (%)	LAM _{NE} (%)	LAM _{PE} (%)	RMSE pOCV (mV)	Q (%)
NMC	0.96	1.54	0.46	21.09 (<0.77%)	1.16
NCA	0.78	1.75	0.40	21.05 (<0.76%)	1.09

6. Conclusions

In this paper, we demonstrate that a generalised CNN-based degradation diagnostic method can rapidly and accurately identify DMs and aging paths for various battery chemistries with three example leading battery types (NMC, LFP, NCA) cycled under different conditions. Our method can automatically extract degradation features from the accessible and reliable ΔQ signal, and quantify battery DMs in 0.012 s, which has significant advantages for the processing of large datasets. Synthetically generated OCV curves from half-cell data allows for the creation of a large training database without the need for costly and time-consuming lifetime experiments. Thus, the rapid nature of our method manifests not only in the high computational efficiency of the CNN but, most importantly, in super low training cost/time. Furthermore, we reveal and prove the underpinning correlations among the thermodynamic DMs, which fundamentally originates from the fact that creating the aged FC OCVs through the scaling and shifting of half-cell OCVs conforms to the superposition principle. For the experimentally aged batteries, we thus propose a non-invasive comprehensive evaluation method for DMQ results. Beyond analysis of the pOCV simulation errors, we also assess three thermodynamic DM errors and all the RMSEs were found to be less than 1.22%. This level of accuracy is achieved by a generic CNN-based diagnostic method which involves almost all aging paths, and the parameterisation of OCV considering the IC and DV errors, as opposed to only OCV errors. We show that the degradation mechanisms of the three batteries are significantly different despite the similar capacity decreasing trend, with the CNN approach providing

deeper insights into the shifting DMs over the lifetime of use.

We also compare the quantified results with those from traditional OCV model parameterization-based diagnostic methods, with the RMSD below 0.72%, implying the high accuracy of the proposed method. Moreover, the CNN approach, which involves only one forward calculation rather than iterative calculations, features fast computation. To demonstrate real-world applicability, we implement the CNN-based diagnostic method with partial discharge/charge data, showing a low deviation of less than 1.75% compared with the results for the full voltage approach. This highlights the promising potential of online diagnosing battery health in the real world.

Overall, this work extends battery degradation theory through a detailed elaboration of the correlation of different DMs and leveraged this understanding towards developing a generic machine learning-based diagnostic method of rapidly quantifying battery degradation. The computationally cheap and fast nature of the diagnostic method makes it a promising approaching for online battery diagnostics and provides a new avenue for intelligent battery control to help prolong battery lifetime and decrease application cost.

7. Methods

7.1. Battery experiments

Three types of leading commercial lithium-ion batteries, i.e. high-power NMC/graphite Kokam pouch cell, high-energy LFP/graphite Wangxiang (A123) pouch cell, and high-energy NCA/graphite Panasonic 18,650 cylindrical cell, were utilized in this work. The NMC, LFP and NCA batteries have a nominal capacity of 7.5 Ah, 50 Ah, and 3Ah, with the cut-off voltage of 2.7 V/4.2 V, 2.5 V/3.65 V, and 2.5 V/4.2 V, respectively. The maximum continuous charge/discharge currents of these three batteries are 0.3C/4C, 0.5C/1C, and 0.5C/3.3C, respectively. The battery testers, Basytec and MACCOR, were employed to conduct the cycling and performance experiments for the NMC battery, and LFP and NCA batteries, respectively. The NMC and NCA batteries were cycled from the fresh state, while the LFP battery was cycled after being used in an electric bus, representing the second use.

The NMC battery was cycled between 2.7 V and 4.2 V with a

constant-current (CC) charge/discharge of 0.3C/5C at a constant ambient temperature of 45 °C inside a thermal chamber with forced air cooling. Before the first cycle and after every 20 cycles, the battery was soaked at 25 °C for more than 3 h and then the performance tests were conducted. The battery was charged at 0.3C until 4.2 V and then charged with constant voltage until the charge current decreased to 0.01C. It was then discharged with 0.3C until 2.7 V. The charge and discharge tests were performed twice. Electrochemical impedance spectroscopy (EIS) was tested with 200 mA in the frequency range of 5 kHz to 10 mHz, with a resolution of 10 points per decade, at 50% SOC and 10 °C before cycling and after cycling completed. The SEM imaging was carried out for the anode and cathode materials harvested by opening the fresh and completely aged cells.

The LFP battery during cycling was charged with 0.5C until 3.65 V and then discharged with 1C until 2.5 V at a constant ambient temperature of 25 °C inside a thermal chamber. The performance tests were conducted before the first cycle and after every 100 or 150 cycles. The battery was discharged at 0.05C until 2.5 V and then rested for 2 h, followed by the 0.05C CC charge until 3.65 V. After resting for 2 h, the battery was discharged at 0.05C until 2.5 V. At 50% and 95% SOCs, EIS tests was conducted with 2A in the frequency range of 10 kHz to 10 mHz, with a resolution of 6 points per decade.

The cycling data of the NCA battery comes from the Oxford battery degradation dataset [51,52]. The NCA battery was subjected to cyclic and calendar aging at 24 °C, i.e. it was periodically exposed to two days of cycling and ten days of calendar aging. During cycling aging, the battery was charged and discharged at 0.5C between 2.5 V and 4.2 V, while during calendar aging the battery rested at 90% SOC. Before the first cycle and after every 48 cycles, the performance test, low current cycling of 1/24C, was performed between 2.5 V and 4.2 V at 24 °C. EIS tests were carried out with 100 mA in the frequency range from 5 kHz to 10 mHz, with a resolution of 6 points per decade at 80%, 50% and 20% SOCs. The capacities of NMC, LFP, and NCA batteries under different cycles are displayed in Supplementary Fig. 20.

The NMC and graphite half cells were assembled using electrode materials harvested from a fresh NMC battery. These half cells are constructed with lithium foil as the counter electrode, LP30 electrolyte consisting of 1.0 M LiPF₆ solution in 50/50 ethylene carbonate and dimethyl carbonate, and Celgard 2400 separator. Pseudo-OCV (pOCV) measurements were conducted on the NMC and graphite half-cells with the CC charge and discharge of 1/30C at 25 °C. The cut-off voltages for NMC and graphite half-cells are 3.0 V/4.4 V and 0.04 V/1.25 V vs. Li⁺/Li, respectively. Analogously, the NCA pOCV was measured with the NCA half-cell collected from the fresh NCA battery [51,52]. The pOCV of the LFP half-cell is obtained from the reference [35].

7.2. OCV model parameterization

We use the pseudo-OCVs (pOCV) of the PE and NE half-cells to construct the FC pOCV [13–15]. The FC pOCV (U_{sim}) can be expressed as:

$$\begin{cases} U_{sim} = U_{PE}(x_{PE}) - U_{NE}(x_{NE}) - IR \\ x_{PE} = x_{PE,0} - \int_0^t \frac{I}{Q_{PE}} d\tau \\ x_{NE} = x_{NE,0} + \int_0^t \frac{I}{Q_{NE}} d\tau \end{cases} \quad (6)$$

where Q_{PE} , Q_{NE} , x_{PE} , and x_{NE} are the available capacity of PE and NE, and the stoichiometric coefficients of PE and NE changed proportionally to the current I , respectively. $x_{PE,0}$ and $x_{NE,0}$ stand for the initial values of x_{PE} and x_{NE} , respectively. The current $I > 0$ denotes a discharge process, while $I < 0$ means a charge process. R represents an additional potential loss for the FC constructed from the half cells of PE and NE, corresponding to the resistance in the FC. U_{PE} and U_{NE} are the pOCVs of the PE

and NE, respectively. We employ the RMSE between the simulation and measurement FC pOCVs to evaluate the simulation accuracy and their RMSE (U_{RMSE}) can be expressed as:

$$U_{RMSE} = \sqrt{\frac{1}{T} \sum_{t=1}^T (U_{sim}(t) - U_{exp}(t))^2} \quad (7)$$

where $U_{exp}(t)$, and T are the measurement pOCV with the sampling interval of 1 s during discharge (charge) and the total time taken in a discharge (charge) process, respectively. When Eq. (7) is used to fit the FC pOCV, some local regions of the simulation pOCV may not agree well with those of the measurement ones. In light of this, to improve the OCV simulation accuracy, we consider the accuracy of differential signals of FC pOCVs, i.e. IC, DV. The RMSEs of simulation and measurement ICs (IC_{RMSE}) and DVs (DV_{RMSE}) deduced from the pOCVs are thus used to evaluate the pOCV simulation accuracy, and they can be expressed as:

$$\begin{cases} IC_{RMSE} = \sqrt{\frac{1}{N_1} \sum_{n=1}^{N_1} (IC_{U_{sim}}(n) - IC_{U_{exp}}(n))^2} \\ DV_{RMSE} = \sqrt{\frac{1}{N_2} \sum_{n=1}^{N_2} (DV_{U_{sim}}(n) - DV_{U_{exp}}(n))^2} \end{cases} \quad (8)$$

where $IC_{U_{sim}}$, $IC_{U_{exp}}$, $DV_{U_{sim}}$, $DV_{U_{exp}}$, N_1 and N_2 stand for the simulation and measurement ICs, the simulation and measurement DVs, and the total data number in the IC and DV, respectively. Therefore, the objective function to parameterize the OCV model can be described as:

$$f_{obj_{ocv}} = \omega_U \cdot U_{RMSE} + \omega_{IC} \cdot IC_{RMSE} + \omega_{DV} \cdot DV_{RMSE} \quad (9)$$

where ω_U , ω_{IC} , and ω_{DV} stand for the weighting coefficients for the RMSEs of pOCV, IC, and DV, respectively, and their values are presented in Supplementary Table 3. Eq. (9) is solved using the particle swarm optimization to obtain the optimal OCV model parameters. The simulation and measurement OCVs, ICs, DVs and their errors for three batteries are illustrated in Supplementary Figs. 22–24.

7.3. Synthetic OCV dataset for CNN training

We assume that the maximum value of every thermodynamic DM was 25% because the thermodynamic DMs generally affect battery available capacity and the maximum capacity loss is usually about 20% at the end of life. The maximum kinetic degradation for the RI was assumed as 125% because the resistance may dramatically increase with aging. In each scenario in Fig. 2a, every thermodynamic DM varied from 0% to 25% with 2.5% increment and the RI changed from 0% to 125% with 6.25% increment. The sum of the amount of three thermodynamic DMs, and the RI amount divided by five was set as less than 75%. As for the Sc2, there were the lithiated LAMs of both PE and NE, which means that the amount of LLI may be mostly negative, and we thus added a bias of -20% to the LLI. Similarly, in Sc3 and Sc4, there were the lithiated LAM of NE and PE, respectively, and we added a bias of -10% to the LLI. With different values of four independent DMs, the dataset for battery degradation included 26,521 independent combinations in each scenario, and we can synthesize 26,521 unique OCVs with the half-cell potentials of PE and NE using Eq. (6) (Supplementary Fig. 4). The synthetic OCV dataset includes almost all aging paths, more than 1 billion degradation paths (Supplementary Note. 3), when the battery capacity loss and resistance increase are less than 20% and 125%, respectively.

7.4. Input data transformation

To highlight the OCV variation with aging, we utilised the capacity differences (ΔQ) between the aged OCVs and the fresh OCV as the CNN input to quantify battery degradation. We considered the FC pOCV as the capacity as a function of voltage. For instance, we considered the

capacity change in the charge/discharge capacity-voltage curves under 10% capacity loss, denoted $\Delta Q_{10\%}(V) = Q_{10\%}(V) - Q_{0\%}(V)$, where the subscripts indicate cycle number, capacity loss, LAM, LLI or RI. To standardize the capacity-voltage data, all FC pOCVs were fitted to a spline function and linearly interpolated [24]. The capacity was fitted as a function of voltage and evaluated at 506 linearly spaced voltage points from maximum discharge (charge) voltage to the discharge (charge) cut-off voltage. These uniformly sized capacity vectors enable straightforward data manipulations, such as subtraction, to obtain $\Delta Q(V)$ under different cycles. We then transformed the 506 data points into a 22×23 matrix and obtained a 2D image to make it feasible as CNN input. The normalization was applied to process the $\Delta Q(V)$ data before feeding it into the CNN. In this work, the min-max normalization method was adopted, which retains the original distribution of the $\Delta Q(V)$ data and all transformed data fall into the range of [0,1]. The maximum and minimum values of the $\Delta Q(V)$ were kept the same in the training dataset, testing dataset and experimental dataset for CNN model input, respectively.

7.5. Convolutional neural network

The CNN in Fig. 3a contains six learned layers: one input layer, three convolutional layers, one fully-connected layer, and one output layer. The CNN input dimension is the same as the input data dimension, 22×23 . The first convolutional layer contains $64 \ 5 \times 5$ kernels convolving with same-padding and stride=1, followed by batch normalization and rectified linear unit (ReLU) activation layers [53,54]. The second and third convolutional layer includes two arms, respectively. The one arm of the second convolutional layer contains $128 \ 1 \times 1$ kernels with stride=2, and the other arm contains two convolutional layers of $128 \ 3 \times 3$ kernels with stride=2, and $128 \ 3 \times 3$ kernels with stride=1. The last two convolutional arms of the second convolutional layer are concatenated and connected to the third convolutional layer. The one arm of the third convolutional layer includes $256 \ 1 \times 1$ kernels with stride=2, and the other arm includes two convolutional layers of $256 \ 3 \times 3$ kernels with stride=2, and $256 \ 3 \times 3$ kernels with stride=1. Each convolutional layer is with same-padding and followed by batch normalization and ReLU activation layers. The last two convolutional arms of the third convolutional layer are concatenated, flattened and fed to four fully-connected layers. Each fully-connected layer contains 18,432 neurons and is connected to the regression output. The four outputs represent four independent DMs.

We randomly partitioned the synthetic dataset to 80% training, and 20% testing. We utilized the Adam optimizer [55] to train the CNN with 50 epochs, and employed a mini-batch of size 512 for efficient learning. This process is regarded as a round of CNN training, and several rounds of training are performed until the RMSEs of testing results of estimated DMs are small [28,50], e.g. thermodynamic DMs and RI are less than 0.1% and 0.2% for NMC battery, respectively. The cost function (L_{loss}) for training the CNN can be described as:

$$L_{\text{loss}} = \sum_{j=1}^4 \omega_j \cdot L_j \quad (10)$$

where L_j and ω_j stand for the cost function, and the weighting coefficient for every output, respectively. We set the weighting coefficients as 1, 2, 1, and 4 for LLI, LAM_{NE}, LAM_{PE} and RI, respectively. The cost function of every output is generally represented by the half mean squared error loss between CNN predictions (X_i) and target values (Y_i) for regression tasks. It can be thus written as:

$$L_j = \frac{1}{2} \sum (Y_i - X_i)^2 \quad (11)$$

We used the RMSE to evaluate the differences between the predicted and target values. All CNN training and testing for three batteries were performed in MATLAB on a single desktop computer with an NVIDIA

Quadro P4000 GPU. All DMQ with experimental data for three batteries using the trained CNN was carried out in MATLAB on a single general laptop computer with an Intel(R) Core(TM) i5-4300 U CPU.

7.6. Comprehensive evaluation for DMQ results

We evaluated the DMQ results using not only the pOCV error but also the capacity error, as shown in Fig. 4c. The RMSEs (ε_{OCV} , ε_Q) between the simulation and experimental pOCVs can be expressed as:

$$\begin{cases} \varepsilon_{\text{OCV}} = \sqrt{\frac{1}{T(C+1)} \sum_{cyc=0}^C \sum_{t=1}^T (OCV_{\text{sim}}(t, cyc) - OCV_{\text{exp}}(t, cyc))^2} \\ \varepsilon_Q = \sqrt{\frac{1}{(C+1)} \sum_{cyc=0}^C (Q_{\text{sim}}(cyc) - Q_{\text{exp}}(cyc))^2} \end{cases} \quad (12)$$

where ε , cyc , Q , and C represent the RMSE or RMSD value, cycle number or aging days, discharge or charge capacity, and the total cycle number or aging days at the end of tests, respectively. Since some DMs have a low influence on the pOCV variation, the deviation of pOCVs due to different DMs may be low (Supplementary Fig. 1), and only using the pOCV and capacity errors are not sufficient to evaluate the accuracy of the quantified DMs (Supplementary Note 4). Thereby, we further assessed the DMQ results leveraging the trained CNNs in Sc2, Sc3, and Sc4. Based on Eq. (4), we compared the quantification results of LAM_{NE} and LAM_{PE} with the corresponding pseudo reference ones (Fig. 4c), termed as LAM_{NE-pR}, LAM_{PE-pR}, which are the average values of the identified LAM_{NE} and LAM_{PE} by the trained CNNs in Sc2, Sc3, and Sc4. The evaluation metrics (their RMSDs) can be described as:

$$\begin{cases} \varepsilon_{\text{LAM}_{\text{NE}}} = \sqrt{\frac{1}{(C+1)} \sum_{cyc=0}^C (\xi_{\text{LAM}_{\text{NE}}}(cyc) - \xi_{\text{LAM}_{\text{NE-pR}}}(cyc))^2} \\ \varepsilon_{\text{LAM}_{\text{PE}}} = \sqrt{\frac{1}{(C+1)} \sum_{cyc=0}^C (\xi_{\text{LAM}_{\text{PE}}}(cyc) - \xi_{\text{LAM}_{\text{PE-pR}}}(cyc))^2} \\ \xi_{\text{LAM}_{\text{NE-pR}}}(cyc) = (\xi_{\text{LAM}_{\text{NE}_2}}(cyc) + \xi_{\text{LAM}_{\text{NE}_3}}(cyc) + \xi_{\text{LAM}_{\text{NE}_4}}(cyc)) / 3 \\ \xi_{\text{LAM}_{\text{PE-pR}}}(cyc) = (\xi_{\text{LAM}_{\text{PE}_2}}(cyc) + \xi_{\text{LAM}_{\text{PE}_3}}(cyc) + \xi_{\text{LAM}_{\text{PE}_4}}(cyc)) / 3 \end{cases} \quad (13)$$

Using Eq. (5), we can further assess the accuracy of quantified LLI (Fig. 4c), and the LLI metric (RMSD) can be expressed as

$$\begin{cases} \varepsilon_{\text{LLI}} = \sqrt{\frac{1}{(C+1)} \sum_{cyc=0}^C (\xi_{\text{LLI}}(cyc) - \xi_{\text{LLI-pR}}(cyc))^2} \\ \xi_{\text{LLI}'_2}(cyc) = \xi_{\text{LAM}_{\text{NE-pR}}}(cyc) + \xi_{\text{LAM}_{\text{PE-pR}}}(cyc) + \xi_{\text{LLI}_2}(cyc) \\ \xi_{\text{LLI}'_3}(cyc) = \xi_{\text{LAM}_{\text{NE-pR}}}(cyc) + \xi_{\text{LLI}_3}(cyc) \\ \xi_{\text{LLI}'_4}(cyc) = \xi_{\text{LAM}_{\text{PE-pR}}}(cyc) + \xi_{\text{LLI}_4}(cyc) \\ \xi_{\text{LLI-pR}}(cyc) = (\xi_{\text{LLI}'_2}(cyc) + \xi_{\text{LLI}'_3}(cyc) + \xi_{\text{LLI}'_4}(cyc)) / 3 \end{cases} \quad (14)$$

Since the resistance in Eq. (6) is not the real resistance in the battery, we would not evaluate the identified RI. But the quantified RI can reflect the kinetic degradation in the battery. With the Eqs. (12)~(14), we can comprehensively evaluate the quantified DMs using five metrics, i.e. not only use the conventional pOCV and capacity metrics, but importantly employ the identified thermodynamic DMs in other scenarios based the newly developed degradation theory.

Data availability

The data that support the work can be found at <https://data.mendeley.com/datasets/fyhwr8rfh4z/1>, and the other data and codes of this study are available upon reasonable request.

Author contributions

H.R. and B.W. conceived the study. H.R., J.C. and W.A. analysed the experimental data and developed the ML model. J.C. carried out some experiments and H.R. collected all the other data. H.R. wrote the paper. All authors discussed the results and commented on the manuscript. B. W. supervised the work.

Declaration of Competing Interest

The authors declare that they have no known competing financial interests or personal relationships that could have appeared to influence the work reported in this paper.

Acknowledgements

This work was kindly supported by the Faraday Institution's Industrial Fellowship (FIIF-013), Innovate UK Battery Advanced for Future Transport Applications (BAFTA) project (104428), the EPSRC Faraday Institution's Multi-Scale Modelling Project (EP/S003053/1, grant number FIRG003), the EPSRC Joint UK-India Clean Energy centre (JUICE) (EP/P003605/1) and the EPSRC Integrated Development of Low-Carbon Energy Systems (IDLES) project (EP/R045518/1). The authors would also like to express special thanks to Nan Xue and Prof. Bingxiang Sun, Beijing Jiaotong University, Dr. Trishna Raj and Prof. David A. Howey, University of Oxford, and Dr. Xuning Feng, Tsinghua University, for sharing the valuable experimental data for this study.

Supplementary materials

Supplementary material associated with this article can be found, in the online version, at [doi:10.1016/j.egyai.2022.100158](https://doi.org/10.1016/j.egyai.2022.100158).

References

- [1] Dunn B, Kamath H, Tarascon J-M. Electrical energy storage for the grid: a battery of choices. *Science* 2011;334:928–35.
- [2] Tomaszewska A, Chu Z, Feng X, et al. Lithium-ion battery fast charging: a review. *eTransportation* 2019;1:100011.
- [3] Zhu Y, Xie J, Pei A, et al. Fast lithium growth and short circuit induced by localized-temperature hotspots in lithium batteries. *Nat Commun* 2019;10:2067.
- [4] Attia PM, Grover A, Jin N, et al. Closed-loop optimization of fast-charging protocols for batteries with machine learning. *Nature* 2020;578:397–402.
- [5] Christensen J, Newman J. Cyclable lithium and capacity loss in Li-ion cells. *J Electrochem Soc* 2005;152:A818.
- [6] Zhao K, Pharr M, Vlassak JJ, et al. Fracture of electrodes in lithium-ion batteries caused by fast charging. *J Appl Phys* 2010;108:073517.
- [7] Barré A, Deguilhem B, Grolleau S, et al. A review on lithium-ion battery ageing mechanisms and estimations for automotive applications. *J Power Sources* 2013; 241:680–9.
- [8] Waldmann T, Iturrondobeitia A, Kasper M, et al. Post-mortem analysis of aged lithium-ion batteries: disassembly methodology and physico-chemical analysis techniques. *J Electrochem Soc* 2016;163:A2149.
- [9] Tanim TR, Paul PP, Thampy V, et al. Heterogeneous behavior of lithium plating during extreme fast charging. *Cell Reports Phys Sci* 2020;1:100114.
- [10] Li J, Murphy E, Winnick J, et al. Studies on the cycle life of commercial lithium ion batteries during rapid charge–discharge cycling. *J Power Sources* 2001;102: 294–301.
- [11] Zhang S, Zhao K, Zhu T, et al. Electrochemomechanical degradation of high-capacity battery electrode materials. *Prog Materials Sci* 2017;89:479–521.
- [12] Pastor-Fernández C, Yu TF, Widanage WD, et al. Critical review of non-invasive diagnosis techniques for quantification of degradation modes in lithium-ion batteries. *Renew Sustain. Energy Rev* 2019;109:138–59.
- [13] Dubarry M, Truchot C, Liaw BY. Synthesize battery degradation modes via a diagnostic and prognostic model. *J Power Sources* 2012;219:204–16.
- [14] Han X, Ouyang M, Lu L, et al. A comparative study of commercial lithium ion battery cycle life in electrical vehicle: aging mechanism identification. *J Power Sources* 2014;251:38–54.
- [15] Birkel CR, Roberts MR, McTurk E, et al. Degradation diagnostics for lithium ion cells. *J Power Sources* 2017;341:373–86.
- [16] Ouyang M, Feng X, Han X, et al. A dynamic capacity degradation model and its applications considering varying load for a large format Li-ion battery. *Appl Energy* 2016;165:48–59.
- [17] Dubarry M, Liaw BY, Chen MS, et al. Identifying battery aging mechanisms in large format Li ion cells. *J Power Sources* 2011;196:3420–5.
- [18] Chahbaz A, Meishner F, Li W, et al. Non-invasive identification of calendar and cyclic ageing mechanisms for lithium-titanate-oxide batteries. *Energy Storage Mater* 2021;42:794–805.
- [19] Dahn HM, Smith AJ, Burns JC, et al. User-friendly differential voltage analysis firmware for the analysis of degradation mechanisms in Li-ion batteries. *J Electrochem Soc* 2012;159:A1405.
- [20] Lewerenz M, Marongiu A, Warnecke A, et al. Differential voltage analysis as a tool for analyzing inhomogeneous aging: a case study for LiFePO₄/graphite cylindrical cells. *J Power Sources* 2017;368:57–67.
- [21] Wu B, Yufit V, Merla Y, et al. Differential thermal voltammetry for tracking of degradation in lithium-ion batteries. *J Power Sources* 2015;273:495–501.
- [22] Merla Y, Wu B, Yufit V, et al. Novel application of differential thermal voltammetry as an in-depth state-of-health diagnosis method for lithium-ion batteries. *J Power Sources* 2016;307:308–19.
- [23] Dubarry M, Bercebar M, Devie A, et al. State of health battery estimator enabling degradation diagnosis: model and algorithm description. *J Power Sources* 2017; 360:59–69.
- [24] Severson KA, Attia PM, Jin N, et al. Data-driven prediction of battery cycle life before capacity degradation. *Nat Energy* 2019;4:383–91.
- [25] Wu B, Widanage WD, Yang S, et al. Battery digital twins: perspectives on the fusion of models, data and artificial intelligence for smart battery management systems. *Energy and AI* 2020;1:100016.
- [26] Zhang Y, Tang Q, Zhang Y, et al. Identifying degradation patterns of lithium ion batteries from impedance spectroscopy using machine learning. *Nat Commun* 2020;11:1–6.
- [27] Lin HT, Liang TJ, Chen SM. Estimation of battery state of health using probabilistic neural network. *IEEE Trans Ind Inform* 2012;9:679–85.
- [28] Shen S, Sadoughi M, Li M, et al. Deep convolutional neural networks with ensemble learning and transfer learning for capacity estimation of lithium-ion batteries. *Appl Energy* 2020;260:114296.
- [29] Li W, Sengupta N, Dechent P, et al. Online capacity estimation of lithium-ion batteries with deep long short-term memory networks. *J Power Sources* 2020;482: 228863.
- [30] Lee S., Kim Y. Li-ion battery electrode health diagnostics using machine learning. 2020 American control conf., 1137–1142 (2020).
- [31] Mayilvahanan K.S., Takeuchi K.J., Takeuchi E.S., et al. Supervised learning of synthetic big data for li-ion battery degradation diagnosis. *Batteries & Supercaps*, (2021).
- [32] Tian J, Xiong R, Shen W, et al. Electrode ageing estimation and open circuit voltage reconstruction for lithium ion batteries. *Energy Storage Mater* 2021;37:283–95.
- [33] Dubarry M, Beck D. Big data training data for artificial intelligence-based Li-ion diagnosis and prognosis. *J Power Sources* 2020;479:228806.
- [34] Kim S, Yi Z, Chen BR, et al. Rapid failure mode classification and quantification in batteries: a deep learning modeling framework. *Energy Storage Mater* 2022;45: 1002–11.
- [35] Feng X, Merla Y, Weng C, et al. A reliable approach of differentiating discrete sampled-data for battery diagnosis. *eTransportation* 2020;3:100051.
- [36] Mohan S, Kim Y, Siegel JB, Samad NA, Stefanopoulou AG. A phenomenological model of bulk force in a li-ion battery pack and its application to state of charge estimation. *J Electrochem Soc* 2014;161:A2222–31.
- [37] Sun S, Guan T, Cheng X, et al. Accelerated aging and degradation mechanism of LiFePO₄/graphite batteries cycled at high discharge rates. *RSC Adv* 2018;8: 25695–703.
- [38] Edge J.S., O'Kane S., Prosser R., et al. Lithium ion battery degradation: what you need to know. *Phys Chem Chem Phys* (2021).
- [39] Ruan H, Sun B, Jiang J, et al. A modified-electrochemical impedance spectroscopy-based multi-time-scale fractional-order model for lithium-ion batteries. *Electrochim Acta* 2021;394:139066.
- [40] Dubarry M, Truchot C, Liaw BY. Cell degradation in commercial LiFePO₄ cells with high-power and high-energy designs. *J Power Sources* 2014;258:408–19.
- [41] Zuo P, Zhao YP. A phase field model coupling lithium diffusion and stress evolution with crack propagation and application in lithium ion batteries. *Phys Chem Chem Phys* 2015;17:287–97.
- [42] Liu P, Wang J, Hicks-Garner J, et al. Aging mechanisms of LiFePO₄ batteries deduced by electrochemical and structural analyses. *J Electrochem Soc* 2010;157: A499.
- [43] Li S, Meng Q, Fan M, et al. Analysis for performance degradation mechanisms of the retired LiFePO₄/graphite power cells. *Ionics (Kiel)* 2020;26:4443–54.
- [44] Bloom I, Cole BW, Sohn JJ, et al. An accelerated calendar and cycle life study of Li-ion cells. *J Power Sources* 2001;101:238–47.
- [45] Wang J, Purewal J, Liu P, et al. Degradation of lithium ion batteries employing graphite negatives and nickel–cobalt–manganese oxide+ spinel manganese oxide positives: part 1, aging mechanisms and life estimation. *J Power Sources* 2014;269: 937–48.

- [46] Dubarry M, Baure G, Devie A. Durability and reliability of EV batteries under electric utility grid operations: path dependence of battery degradation. *J Electrochem Soc* 2018;165:A773.
- [47] Keil P, Jossen A. Calendar aging of NCA lithium-ion batteries investigated by differential voltage analysis and coulomb tracking. *J Electrochem Soc* 2016;164:A6066.
- [48] Keil J, Jossen A. Electrochemical modeling of linear and nonlinear aging of lithium-ion cells. *J Electrochem Soc* 2020;167:110535.
- [49] Gao Y, Jiang J, Zhang C, et al. Aging mechanisms under different state-of-charge ranges and the multi-indicators system of state-of-health for lithium-ion battery with Li(NiMnCo)O₂ cathode. *J Power Sources* 2018;400:641–51.
- [50] Tian J, Xiong R, Shen W, et al. Deep neural network battery charging curve prediction using 30 points collected in 10min. *Joule* 2021;5:1521–34.
- [51] Raj, T., Howey, D., <https://ora.ox.ac.uk/objects/uuid:de62b5d2-6154-426d-bcbb-30253ddb7d1e>. DOI:10.5287/bodleian:v0ervBv6p.
- [52] Raj T, Wang AA, Monroe CW, et al. Investigation of path-dependent degradation in lithium-ion batteries. *Batteries & Supercaps* 2020;3:1377–85.
- [53] Krizhevsky A, Sutskever I, Hinton GE. Imagenet classification with deep convolutional neural networks. *Adv Neural Inf Process. Syst* 2012;25:1097–105.
- [54] Glorot, X., Bordes, A., Bengio, Y. Deep sparse rectifier neural networks. In *Pro. 14th international conference on artificial intelligence and statistics* 315–23 (2011).
- [55] Kingma D.P., Ba J. Adam: A method for stochastic optimization. *arXiv preprint arXiv:1412.6980*, (2014).